Vortex Simulation of a Three-Dimensional Reacting Shear Layer with Infinite-Rate Kinetics

Omar M. Knio* and Ahmed F. Ghoniem†
Massachusetts Institute of Technology, Cambridge, Massachusetts 02139

The three-dimensional transport element method is extended to solve the conservation equations for reacting flow. The numerical scheme belongs to an adaptive, Lagrangian class of field methods in which computational effort is concentrated in zones of finite vorticity and chemical reaction. We use the low Mach number approximation of combustion and restrict our attention to the case of diffusion flames with no heat release. A single-step, second-order, infinite-rate kinetics chemical reaction model is employed. The scheme is applied to study the effect of flow-induced instabilities on the reaction field in a temporal shear layer. Results are obtained in the high Peclet number regime for a wide range of Damkohler numbers. Changes in the reaction field are related to either the entrainment or the strain field associated with the saturation of the instabilities. With increasing Damkohler number, the reaction region changes from a distributed zone embedded within spanwise and streamwise vortices to a thin sheet surrounding their cores. The product concentration always exhibits strong similarity to the vorticity distribution, realizing its highest values in zones of high vorticity and falling rapidly in regions where the vorticity is small. Variation of the Peclet number yields minor changes in the product distribution and in the reaction zone structure, but strongly affects product formation rates.

I. Introduction

THE subject of this work is the construction of Lagrangian field methods for the numerical simulation of three-dimensional, high Reynolds number, reacting shear flow. In this fluid flow regime, vorticity is confined to a small well-defined fraction of the flowfield making vortex methods, in which computational elements are used to cover the support of vorticity, a natural candidate for the solution of the momentum equation. In previous efforts,[1-3] a modified vortex element scheme was constructed and applied to study the motion of unconfined, inviscid vortex rings. The study revealed the need for 1) a careful representation of the vorticity field at the initial state, and 2) an accurate implementation of numerical schemes as time evolves. These requirements are especially critical in three-dimensional flows where several forms of rapidly growing instabilities of complex shapes are present. To satisfy these requirements, and to accommodate the solution of scalar conservation equations, an adaptive class of Lagrangian field methods, called transport element methods, was constructed. A numerical study of several forms of these methods, which focused on the solution of the inviscid scalar transport equation, was successfully conducted in Refs. 4 and 5.

Although the ultimate goal of this work consists of the construction of numerical methods for the solution of the compressible, turbulent combustion equations, in this study we limit our attention to the low Mach number, isothermal flow limit. In the presence of an exothermic reaction, analysis of burning rates is complicated by the expansion field and the baroclinic vorticity generation spawned by the heat release; the burning rates exhibit higher sensitivity to the strain field. In a three-dimensional flow, these mechanisms are further compounded by vorticity stretching, and individual effects become hard to isolate. By virtue of our simplifying assumptions, computed results will allow us to focus on studying the deformation of the diffusion flame by a known flowfield.

The numerical scheme is obtained by modifying the transport element method discussed in Ref. 5. It is based on the discretization of both vorticity and species concentrations into a number of transport elements of finite, spherically symmetric overlapping cores. Transport elements are distributed over entire material surfaces whose motion is tracked in a Lagrangian frame of reference. Vorticity associated with the elements changes by stretching and tilting, whereas species concentrations are updated by numerically accounting for diffusion-reaction terms. The rotational velocity field is computed by a discrete, desingularized Biot-Savart convolution over the field of the elements. Boundary conditions are satisfied by adding the contribution of the appropriate image system of the transport elements.

The method is applied to study the evolution of chemically reacting temporal shear layers. The flowfield is selected because of 1) its practical importance in a large class of combustion problems, and 2) the existence of experimental[6-10] and analytical[11-12] results that focus on the three-dimensional behavior of the flow. However, numerical studies of scalar entrainment, mixing, and chemical reaction in three-dimensional layers remain scarce.[13-16] Thus, the method is used to study the effect of vorticity-induced entrainment and strain on the evolution of diffusion flames. Computed results are obtained for a wide range of Damkohler numbers in order to study its effect on the structure of the reaction zone and product distribution.

II. Formulation and Numerical Scheme

A. Formulation and Governing Equations

We consider a three-dimensional, chemically reacting flow in the limits of infinite Reynolds number, vanishingly small Mach number, and heat release. The reaction is described by a single-step, second-order, infinite-rate kinetics, F (fuel) + O (oxidizer) → P (products). The reactants and products are assumed to behave as perfect gases with equal molecular weights, and equal and constant physical properties. Under these assumptions, the vorticity form of the momentum equation, the continuity, and species conservation equations, nor-

---

Presented as Paper 90-0150 at the AIAA 28th Aerospace Sciences Meeting, Reno, NV, Jan. 8-11, 1990. Received May 21, 1990; revision received Oct. 20, 1990; accepted for publication Oct. 22, 1990.

*Postdoctoral Associate, Department of Mechanical Engineering. Member AIAA.

†Associate Professor, Department of Mechanical Engineering. Member AIAA.

malized with respect to the appropriate combination of velocity U_0, length L_0, and density ρ_0, scales, reduce to

$$\frac{D\boldsymbol{\omega}}{Dt} = \boldsymbol{\omega} \cdot \nabla \boldsymbol{u} \tag{1}$$

$$\nabla \cdot \boldsymbol{u} = 0 \tag{2}$$

$$\frac{Ds^i}{Dt} = \frac{1}{Pe\ Le} \nabla^2 s^i - W \tag{3}$$

where $\boldsymbol{u} = (u,v,w)$ denotes the velocity vector in a right-handed Cartesian system $\boldsymbol{x} = (x,y,z)$, $\omega = \nabla \cdot \boldsymbol{u}$ is the vorticity, t the time, $D/Dt = \partial/\partial t + \boldsymbol{u} \cdot \nabla$ the material derivative, $\nabla = (\partial/\partial x, \partial/\partial y, \partial/\partial z)$ the gradient operator, ∇^2 the Laplace operator, $Pe = U_0/(\alpha L_0)$ the Peclet number, $Le = \alpha/\beta$ the Lewis number, and α and β denote the thermal and mass diffusivities, respectively. The model requires the transport of two scalars, s^i $i = 1{,}2$, where $s^1 = c_O$ denotes the oxidizer concentration, whereas $s^2 = c_F$ represents the fuel concentration. The product distribution is given by $c_P = 1 - c_O - c_F$, and chemical production term $W = Da c_O c_F$, where Da is the Damkohler number. Equations (1–3) are obtained by simplifying the low Mach number equations for combustion for vanishingly small heat release. The assumption of no heat release implies that both temperature and density remain constant, so that both baroclinic vorticity generation and volumetric expansion effects cancel in the vorticity transport equation. The model ignores viscous effects since viscosity only affects the motion of the vorticity field well beyond the mixing transition, a mechanism that is not in the scope of the present computations. Mass diffusion effects are retained because they govern the mixing and chemical reaction processes.[17]

B. Numerical Scheme

The numerical scheme used in the solution of the governing equations is obtained by extension of the methods analyzed in previous work[5] and, hence, is summarized in the following. Its construction starts with the discretization of the vorticity field $\boldsymbol{\omega}(\boldsymbol{x})$ on a three-dimensional mesh:

$$\boldsymbol{\omega}(\boldsymbol{x},0) = \sum_{i=1}^{N} \boldsymbol{\omega}_i(0)\, dV_i\, f_\delta(\boldsymbol{x} - \boldsymbol{X}_i) \tag{4}$$

where N is the total number of vortex elements, and $\boldsymbol{X}_i$, dV_i, and $\boldsymbol{\omega}_i$ denote the center, volume, and vorticity of element i, respectively. The vorticity associated with each element is smoothed in a small neighborhood of $\boldsymbol{X}_i$ according to a spherical core function f_δ with core radius δ, where $f_\delta(r) = (1/\delta^3) f(r/\delta)$. A third-order Gaussian core function,

$$f(r) = \frac{3}{4\pi} e^{-r^3} \tag{5}$$

is adopted.[18,19] Note that f decays rapidly for $r > \delta$ so that δ represents the radius of the sphere where vorticity is concentrated.

The vortex elements are initialized by employing entire material surfaces distributed within the support of vorticity. The surfaces are discretized into rectangular transport elements that generalize the notion of the vortex vector elements. In this representation, a transport element is specified by the vector $(\boldsymbol{\chi}_i^1, \boldsymbol{\chi}_i^2, \boldsymbol{\chi}_i^3, \boldsymbol{\chi}_i^4)$, where the Lagrangian coordinates $\boldsymbol{\chi}_i^1$, $\boldsymbol{\chi}_i^2$, $\boldsymbol{\chi}_i^3$, and $\boldsymbol{\chi}_i^4$ are used to define a rectangular area around its center. The transport elements are selected such that the sides of adjacent rectangles coincide to form a mesh that continuously describes an entire material surface. This construction resembles but differs from that proposed by Agishtein and Migdal[20] who used triangular elements to describe a singular vortex sheet.

Within each element, we use a finite element description of the surface using linear interpolation functions.[21] The motion of the centers of the elements $\boldsymbol{\chi}_i$ is approximated by

$$\boldsymbol{\chi}_i(t) = \tfrac{1}{4}[\boldsymbol{\chi}_i^1(t) + \boldsymbol{\chi}_i^2(t) + \boldsymbol{\chi}_i^3(t) + \boldsymbol{\chi}_i^4(t)] \tag{6}$$

where the $\boldsymbol{\chi}_i^j(t)$, $j = 1{,}2{,}3{,}4$, denote the instantaneous coordinate of the material particles whose Lagrangian coordinates coincide with the vertices of the initial mesh. This representation accommodates the integration of the vorticity transport equation, which is necessary in general flow situations,[5] but retains the advantages of vortex element schemes, which relate the evolution of the vorticity field to the deformation of vortex lines.[22–26] Under the assumptions made earlier, the latter approach is preferred since it results in considerable computational savings as direct evaluation of the gradient of the flow map is avoided. This is done by associating with each element a circulation Γ_i and requiring that the pair of opposing sides of the rectangles $(\boldsymbol{\chi}^3, \boldsymbol{\chi}^1)$ and $(\boldsymbol{\chi}^4, \boldsymbol{\chi}^2)$ align with the local vorticity vector. The quantity $\boldsymbol{\omega}_i(t) dV_i$ is thus replaced by $\Gamma_i \delta\boldsymbol{\chi}_i(t)$, where the evolution of the material length $\delta\boldsymbol{\chi}_i(t)$ is given by

$$\delta\boldsymbol{\chi}_i(t) = \tfrac{1}{2}[\boldsymbol{\chi}_i^3(t) + \boldsymbol{\chi}_i^4(t) - \boldsymbol{\chi}_i^1(t) - \boldsymbol{\chi}_i^2(t)] \tag{7}$$

According to Kelvin's theorem, Γ_i remains constant along a particle path, whereas Helmholtz's theorem is used to relate the evolution of $\boldsymbol{\omega}_i(t)$ to that of $\delta\boldsymbol{\chi}_i(t)$ as follows,

$$\boldsymbol{\omega}_i(t) = \frac{|\boldsymbol{\omega}_i(0)|}{|\delta \boldsymbol{X}_i|} \delta\boldsymbol{\chi}_i(t) \tag{8}$$

The velocity field, induced by the vorticity distribution in an infinite domain, is given by the discrete, desingularized Biot-Savart law:

$$\boldsymbol{u}_\omega = \frac{1}{4\pi} \sum_{i=1}^{N} \Gamma_i \frac{(\boldsymbol{x} - \boldsymbol{\chi}_i) \times \delta\boldsymbol{\chi}_i}{|\boldsymbol{x} - \boldsymbol{\chi}_i|^3} \kappa\left(\frac{r_i}{\delta}\right) \tag{9}$$

where

$$\kappa(r) = 4\pi \int_0^r f(r')\, r'^2\, dr' = 1 - \exp(-r^3)$$

and $r_i = |\boldsymbol{x} - \boldsymbol{\chi}_i|$. The velocity field thus obtained is used in conjunction with a second-order predictor-corrector scheme to update the particle positions $\boldsymbol{\chi}_i^j(t)$.

Analysis of particle methods,[22–26] and numerical evidence[5] indicate that severe deformation of the Lagrangian mesh under the action of the strain field causes a deterioration in the discretization accuracy. To overcome this difficulty, the remeshing algorithm suggested in Ref. 5 is utilized. It effectively amounts to the redistribution of the elements along a vortex tube and the splitting of the vortex tubes along material surfaces whenever the length of the elements exceeds the core radius. This allows us to capture severe distortions of the flow without losing accuracy.

The numerical solution of Eq. (3) is performed in a similar way as that of the vorticity field. The concentration fields are discretized among the transport elements, which now carry, along with vorticity, discrete local values of s^1 and s^2. We let

$$s(\boldsymbol{x},t) = \sum_{i=1}^{N} s_i(t)\, dV_i\, f_\delta[\boldsymbol{x} - \boldsymbol{\chi}_i(t)] \tag{10}$$

Next, we adopt the discrete approximation of the Laplacian operator:

$$\nabla^2 s_j \sim B(s_j) = \frac{2}{\delta^2} \sum_{k=1}^{N} (s_k - s_j)\, dV_k\, g_\delta\, [\boldsymbol{\chi}_k(t) - \boldsymbol{\chi}_j(t)] \tag{11}$$

where

$$g(r) = -\frac{1}{r}\frac{\mathrm{d}f}{\mathrm{d}r}, \qquad g_\delta(\boldsymbol{x}) = \frac{1}{\delta^3}\, g\left(\frac{|\boldsymbol{x}|}{\delta}\right) \tag{12}$$

and f is the core smoothing function previously defined.[27–31] This scheme is preferred over random walk methods,[32] whose implementation is cumbersome in conjunction with the transport of connected surfaces, and over core spreading techniques,[33] which no longer yield simple evolution equations for the core radii. The evolution of the scalar concentration fields is found by numerically integrating

$$\frac{\mathrm{d}s_i^j}{\mathrm{d}t} = \frac{1}{Pe\, Le} B(s_i^j) + W \tag{13}$$

using the same method employed in tracking the particle positions.

III. Flow Geometry and Initial Conditions

We assume a vorticity layer of finite thickness, periodic in its streamwise x direction and spanwise y direction, and unconfined in the cross-stream z direction. The thickness of the layer is expressed by 2σ, where σ is the standard deviation of the second-order Gaussian curve, which describes the physical vorticity distribution within the layer at $t = 0$. Letting $\Omega(\underline{x})$ denote this initial condition, we have $\Omega_y(\boldsymbol{x}) = 2/(\sigma\sqrt{\pi})\exp(-z^2/\sigma^2)$, $\Omega_x(\boldsymbol{x}) = \Omega_z(\boldsymbol{x}) = 0$. The corresponding velocity distribution $\boldsymbol{U}(\boldsymbol{x})$ at $t = 0$ is given by $V(\boldsymbol{x}) = W(\boldsymbol{x}) = 0$, and $U(\boldsymbol{x}) = \mathrm{erf}(z/\sigma)$, erf being the error function. The vorticity layer thus admits a streamwise velocity difference $\Delta U = 2$. The periodicity length in the x direction, $\lambda_x = 13.2\ \sigma$, corresponds to the wavelength of the two-dimensional most unstable mode,[11] whereas $\lambda_y = \lambda_x/2$ is selected close to the wavelength of the most amplified three-dimensional mode.[12] The initial fuel and oxidizer concentrations follow error-function-type profiles, $c_O(t=0) = \mathrm{erf}(z/\sigma)$, $c_F(t=0) = 1 - \mathrm{erf}(z/\sigma)$, so that $c_P(t=0) = 0$. Thus, the top stream and bottom streams consist, respectively, of oxidizer and fuel, and the initial thickness of the vorticity layer matches the mixed zone, or the zone of finite chemical activity.

The layer is initially discretized among elements distributed on a grid of 20 × 14 × 5 points along the x, y, and z directions, respectively. Furthermore, σ is chosen as a reference length scale so that $\Delta x = \Delta z = 0.66$ and $\Delta y = 0.471$. The top stream velocity, $U(z \to \infty)$, is selected as a reference velocity scale, the time step $\Delta t = 0.1$, and $\delta = 0.89$. The circulations of the elements are found by matching discretized and assumed vorticity values at the centers of the elements, whereas the concentration fields s_i^1 and s_i^2 are initialized by associating with the transport elements, the values realized by the corresponding physical distribution at their centers. Normal, periodic boundary conditions are satisfied by adding the contribution of the image system of the transport elements, using the procedure detailed in Ref. 5.

The layer is perturbed at $t = 0$ using two sine waves of the same amplitude in the streamwise and spanwise directions, as expressed by the transformation $z_i \to z_i + \varepsilon\sin(2\pi x_i/\lambda_x) + \varepsilon\sin(2\pi y_i/\lambda_y)$, $\varepsilon = 0.02\ \lambda_x$. Computations of the nonreacting flowfield are carried until $t = 18.0$ to observe the growth of two- and three-dimensional instabilities, whereas those of the reacting flowfield are stopped at $t = 16.0$, i.e., when mature vortical structures are formed. Results are obtained for a total of 21 cases, assuming infinite Reynolds number, unit Lewis number, and varying the Damkohler and Peclet numbers. We consider seven values of the Damkohler number, $Da = 0.1$, 0.2, 0.4, 1.0, 2.5, 5.0, and 10.0, and three values of the Peclet number, $Pe = 250$, 500, and 1000. In the following, we start with a summary of the evolution of the flowfield and vorticity field and then discuss the influence of the vortical structures on the shape of the reaction zone and the product concentration distribution.

IV. Flowfield Evolution

The development of the shear layer, as represented by the evolution of the material surfaces where the vorticity is nonzero (the flow is inviscid), and the vorticity field on different spanwise and streamwise locations are examined. Similar flow configurations were analyzed by the present authors in Ref. 5, studied by Ashurst and Meiburg,[34] who focused on the dynamics of vortex filaments in both symmetric and asymmetric layers, and by Metcalfe et al.,[35] who used a spectral scheme to examine the evolution of individual instability modes. Hence, the main features of the flow are briefly discussed in the following.

Figures 1 depict three-dimensional perspective views of the material surface initially located at $z = 0$, and $t = 12.0$ and 16.0. This represents the middle surface within the shear layer where most of the vorticity is concentrated. The plots are

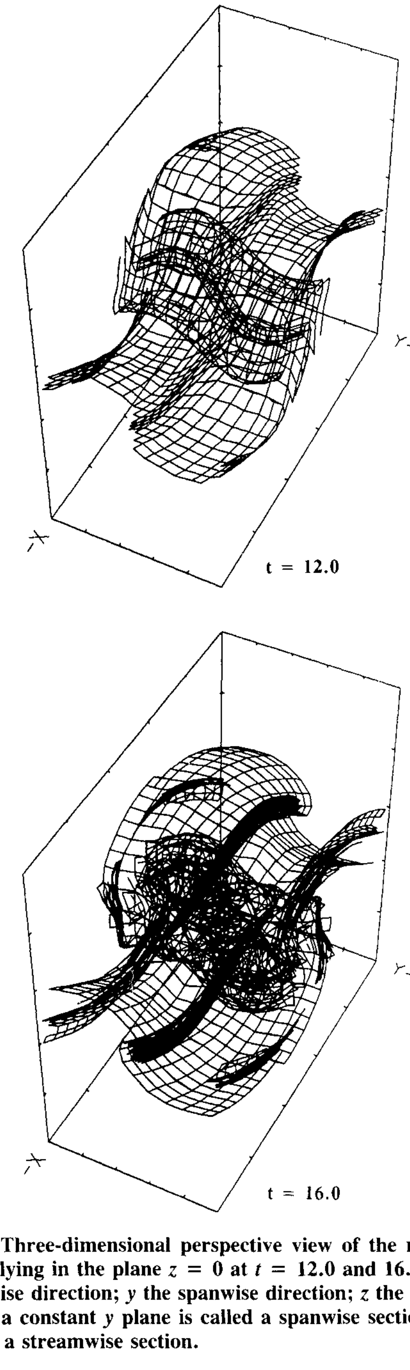

Fig. 1 Three-dimensional perspective view of the material surface initially lying in the plane $z = 0$ at $t = 12.0$ and 16.0: x denotes the streamwise direction; y the spanwise direction; z the cross-stream direction; a constant y plane is called a spanwise section; a constant x is called a streamwise section.

generated from the point of view of an observer located at (48,24,48).

At $t = 12.0$, the rollup of the vorticity layer produces a well-defined spanwise eddy core. The saturation of the instability is associated with the redistribution of the vorticity field and results in the creation of a core where most of the spanwise vorticity is concentrated and braids, which are constantly strained under the influence of the spanwise vortex cores. The amplitude of the spanwise perturbation is significantly amplified along the core, an indication of the evolution of the translative instability.[12] This nonuniform axial displacement of the core is accompanied by an out-of-phase deformation of the braids region under the influence of the generated streamwise vorticity.

At $t = 16.0$, the motion becomes highly three dimensional as differences along various spanwise stations become important and depart from the shape of the imposed sine-wave perturbation. The stretching of the braids, which are anchored along the boundaries of the domain and pulled toward the core, leads to the generation and intensification of streamwise vorticity. This results in the saturation of the streamwise vorticity into vortex rods, which extend throughout the braids and are wrapped around the spanwise core. The presence of streamwise vortex rods is inferred from the spinning of material surfaces about streamwise axes that are located at the spanwise midsection and boundaries of the domain.

The Lagrangian description of the flow is completed by considering two-dimensional cross sections of the computational surfaces. Figures 2 show cross sections through all of the material surfaces at $t = 18.0$. We consider spanwise sections along two-dimensional planes specified by $y = 3.3$ (Fig. 2a) and $y = 1.6$ (Fig. 2b) and streamwise sections through the core and braid regions in the planes located at $x = 6.6$ (Fig. 2c) and $x = 2.0$ (Fig. 2d). Circles are drawn to mark the intersection points with the transport elements. The radius of the circles is smaller than the core radii of the smoothing functions.

The spanwise cross sections illustrate the effect of the translative instability, which causes a nonuniform axial deformation of the spanwise vorticity core. The eddy core is pushed upward and in the direction of the top stream in the left half of the domain, $0 < y < 3.3$, while it suffers an antisymmetric deformation in the other half. The core region at most spanwise cross sections loses its symmetry, as computational elements migrate in the direction opposite to that of the core translation. The intersection of material surfaces with the plane $y = 3.3$ shows that the braids thicken significantly at this spanwise location and that they entrain irrotational fluid from both free streams. This can be verified by simultaneously examining Fig. 2c, which shows the wrapping of the mushrooms around the core of the eddy. The entrainment of mushrooms, which are generated in the braids, toward the core region leads to the formation of a double structure. Dark areas that appear along the core region correspond to the intersection of the streamwise vortex rods with the plane of the figure.

Figures 3–6 show constant spanwise vorticity contours, plotted in two spanwise sections, $y = 3.3$ and 1.6, and streamwise vorticity contours in the streamwise sections $x = 6.6$ and 2.0, respectively. Contours are generated at times $t = 12.0$ and

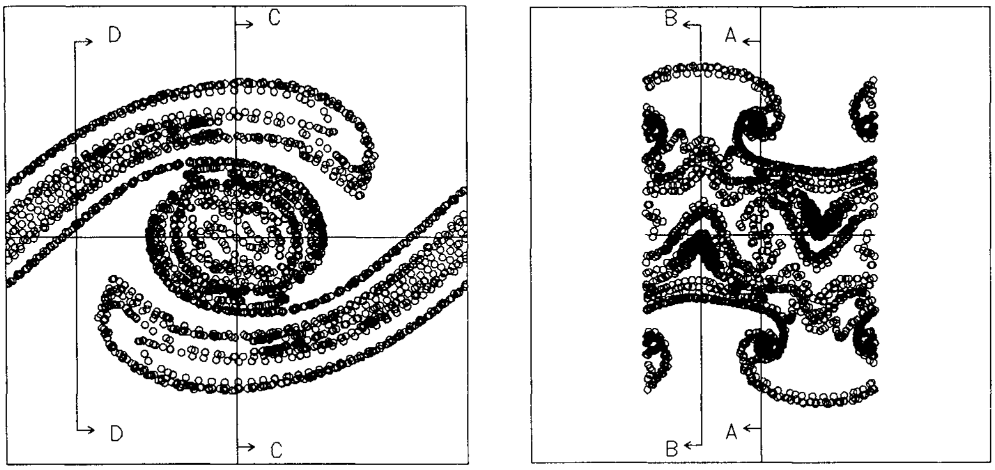

a) y = 3.3, (AA)

c) x = 6.6, (CC)

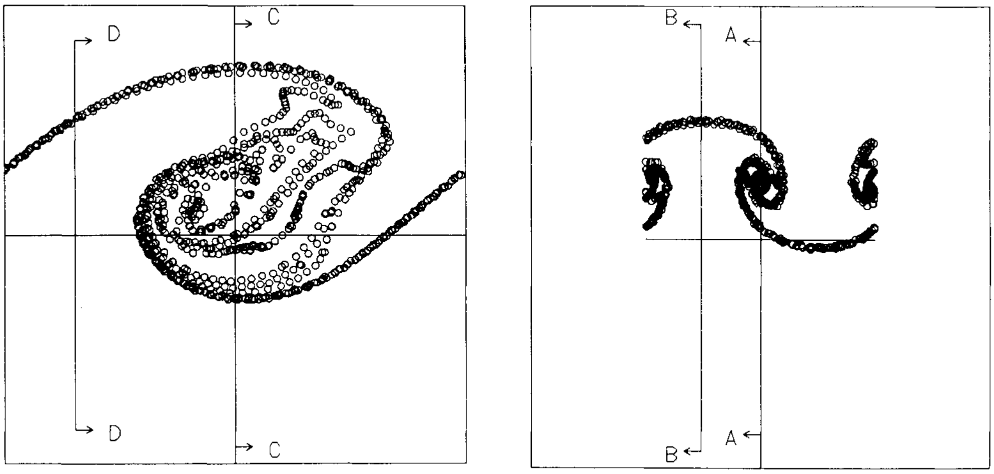

b) y = 1.6, (BB)

d) x = 2.0, (DD)

Fig. 2 Intersection of the Lagrangian mesh at $t = 18.0$: a) $y = 3.3$; b) $y = 1.6$; c) $x = 6.6$; d) $x = 2.0$.

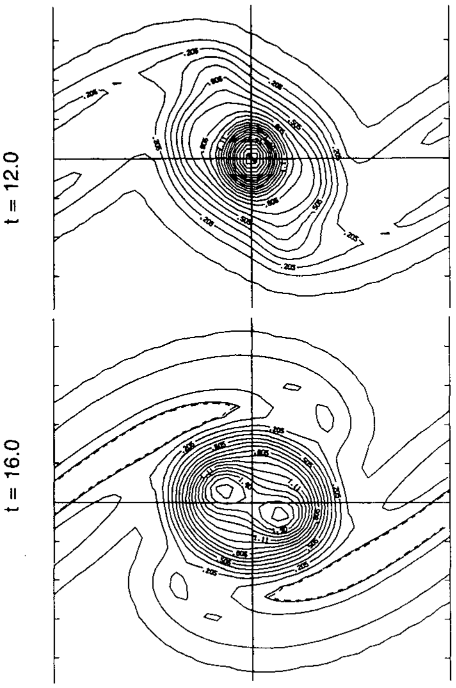

Fig. 3 Contours of the spanwise vorticity ω_y shown in the x-z plane located at $y = 3.3$ at $t = 12.0$ and 16.0: dashed lines are used to represent negative values.

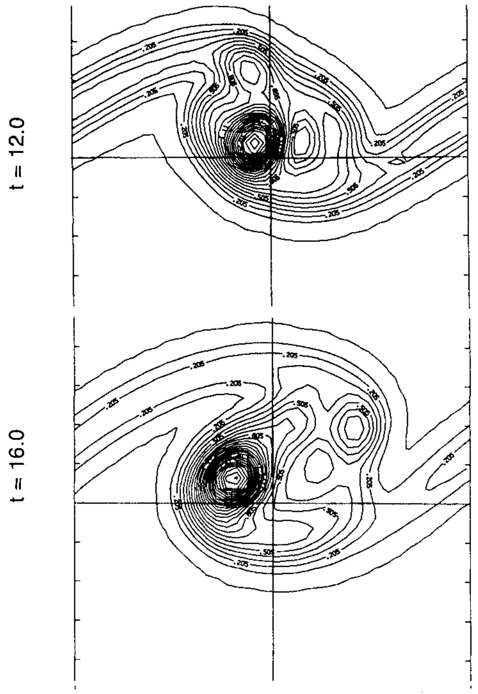

Fig. 4 Contours of the spanwise vorticity ω_y shown in the x-z plane located at $y = 1.6$ at $t = 12.0$ and 16.0.

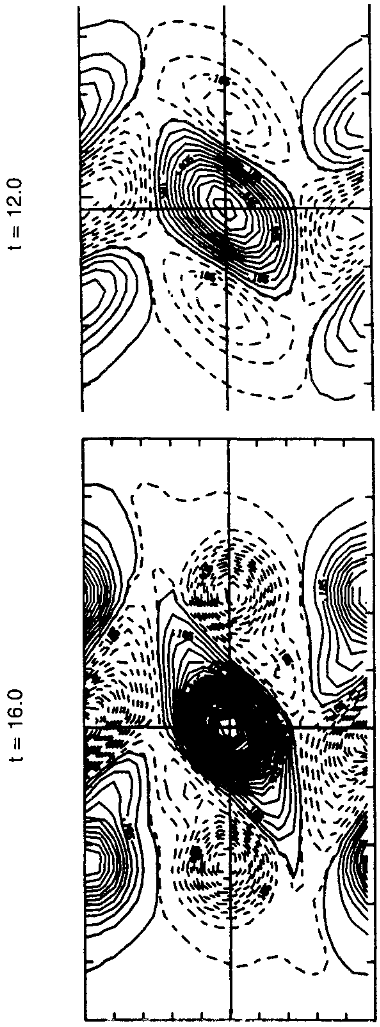

Fig. 5 Contours of the streamwise vorticity ω_x shown in the y-z plane located at $x = 6.6$ at $t = 12.0$ and 16.0.

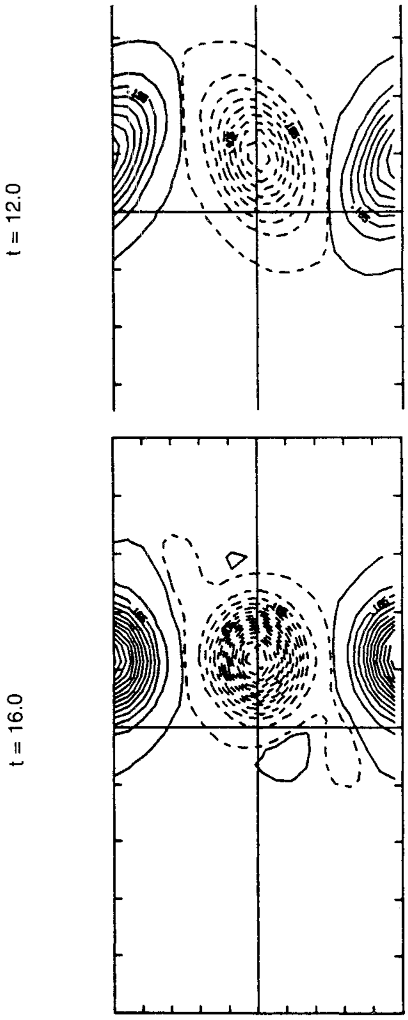

Fig. 6 Contours of the streamwise vorticity ω_x shown in the y-z plane located at $x = 2.0$ at $t = 12.0$ and 16.0.

16.0. At earlier times, the vorticity field exhibits small deviations from that obtained in a two-dimensional flow and, hence, is not depicted. The growth of three-dimensional perturbations is suppressed during the initial stages of the Kelvin-Helmholtz instability, and the spanwise vorticity remains essentially uniform across the layer.[5,34,35] Weak streamwise structures are generated by local tilting of the vortex lines into the streamwise direction, but do not significantly affect the evolution of the flow. This mechanism leads to the creation of zones of alternating streamwise vorticity whose locations and signs follow the shape of sine-wave perturbation.

Following the rollup of the spanwise vorticity, the flowfield undergoes a rapid transition to three-dimensional motion. In the braids region, a violent increase in the amount of streamwise vorticity is observed. The streamwise structure almost doubles in strength in half the time span it took to generate it. This behavior is expected since the creation of the large spanwise eddy results in larger strain rates in the neighborhood of the stagnation lines that anchor the braids.

In the meantime, the streamwise vorticity distribution along the core becomes distinguished by the presence of a top and a bottom row of counter-rotating streamwise vortices. These rows are separated by a third, middle row, which is generated as a result of the growth of perturbations along the core itself by the mechanism of the translative instability and is 180 deg out of phase with the other two.[34] The growth of perturbations along the core leads to a more dramatic increase of the streamwise vorticity as the middle row of vortices becomes stronger than the top and bottom rows. The generation of strong streamwise structures in the core region is not associated with large-amplitude deformation in the streamwise direction. This may be explained by noting that the rollup of the layer, which precedes the three-dimensional motion, forces the migration of the spanwise vorticity from the thinning braids into the core region. Also note that the intensification of the streamwise vortices, entrained from the braids into the cores (the top and bottom rows), lags that observed in the braids. Thus, streamwise vorticity associated with the vortex rods is generated in the braids and then strained toward the cores.

The transition to three-dimensional motion, in its initial stage, does not lead to significant qualitative modification of the structure of the layer as perceived in two-dimensional spanwise cuts. The spanwise vorticity distribution still bears a striking resemblance to that observed in a two-dimensional flow. However, we note two minor differences: 1) the vortex core suffers a reduction of its cross section, although it is essentially governed by the dynamics of the primary instability; and 2) the vorticity distribution loses its symmetry in the plane located at $y = 1.6$, but remains symmetric at the spanwise midsection of the domain $y = 3.3$. The first effect is a consequence of the growth of the three-dimensional perturbation on the spanwise core, which necessitates a stretch component along its axis. The loss of symmetry, which becomes more obvious in the later stages of development of the three-dimensional instability, is discussed later.

The nonlinear stages of evolution of the three-dimensional instability are examined first in the streamwise planes of the shear layer, Figs. 5 and 6. The stretching of the vorticity lines along the braids leads to the maturation of the elongated vortices into round concentrated cores.[36,37] The flowfield induced by the vortex rods causes further deformation of the material surfaces in a spinning motion around their centers and the generation of mushroom structures similar to those experimentally observed.[6-10] The streamwise vorticity in the core region also intensifies. Figure 5 shows the presence of three rows of vortices. The top and bottom rows, characterized by almost circular cores, are associated with the entrainment of vortex rods generated within the braids around the spanwise core, whereas the middle row, generated by the deformation of the core, has elliptical-like eddies with their major axes at 45 deg with respect to the spanwise direction.

The three-dimensional flowfield induced by the amplification and maturation of three-dimensional instabilities leads to significant spanwise variations. The asymmetry in the vorticity distribution originates from the nonuniform displacement of the vorticity cores at different spanwise locations. The center of the core moves in the opposite direction to that of its outer radial stations that define the boundaries. This is in agreement with the results of the three-dimensional linear stability theory of the developed vorticity layer, which predicts a translative instability of the cores in the manner described earlier.[12]

The core deformation resembles that observed in the evolution of the eigenfunctions of the linear stability problem of vortex rings,[38] which predicts a similar behavior for locally curved vortex cores. Detailed analysis of the associated fluid motion[5] shows that this results in preferential entraiment of irrotational fluid from the freestreams.[10] When the core is displaced upward ($0 < y < 3.3$), it entrains more fluid from the bottom stream, whereas the cores that are pushed downward consist mainly of the top stream fluid.

The asymmetry is not present at the spanwise midsection of the domain where the curvature of the eddy vanishes. However, the spanwise vorticity core appears to be formed of two distinct eddies, a configuration that resembles, but is different from, the two-dimensional pairing of vortices. This type of distribution should be contrasted with that obtained in unstable vortex rings, which displays similar features at certain azimuthal cross sections.[2]

V. Reacting Shear Layer

We turn our attention to the study of diffusion flames in three-dimensional vorticity layers. Since heat release effects are neglected, temperature and density remain constant and the reaction does not affect the flowfield. Results are used to analyze the effect of vorticity-induced entrainment and strain on the reaction zone, product distribution, and burning rates. We start with a reacting layer at low Damkohler number and low diffusion, $Da = 0.1$ and $Pe = 1000$, then at high Damkohler number and low diffusion, $Da = 10$ and $Pe = 1000$.

Results are shown in terms of shaded contours of product concentration and product formation rate W. Product concentration is shown in terms of six different shades of gray, mapped to equal size intervals between 0 and 1. The product formation rates are first normalized by the maximum value achieved in the plane where the figure is generated, before the contours are drawn. In these plots, dark areas highlight the zone of highest chemical activity and must not be used as indication of the actual formation rates.

A. Reacting Layer at Low Damkohler Number

Figures 7–10 show product concentration and reaction rate contours in the planes $y = 3.3$ and 1.6 and $x = 6.6$ and 2.0, respectively, generated at $t = 12.0$ and 16.0. In each figure, product concentration and reaction rate contours are shown side by side. At earlier stages, $t \leq 8.0$, examination of the reaction field (not shown here) exhibits small differences from those one obtains in a two-dimensional field.[39,40] The products of reaction and the zone of highest chemical activity surround the region of highest vorticity. Three-dimensional effects are weak in this stage and can only be detected along the streamwise sections, which show very small spanwise undulations of the layer.

With the intensification of the streamwise vortices in the braids and the amplification of the translative instability in the cores, significant deviations from two-dimensional behavior are observed. At $y = 3.3$, the streamwise vortex rods that start to form at the boundaries of the domain enlarge the product concentration layer at this location. As shown in Fig. 7b, enlargement of the layer is a consequence of burning enhancement, associated with the rollup of the surfaces around the streamwise vortices. This is contrary to the result of two-

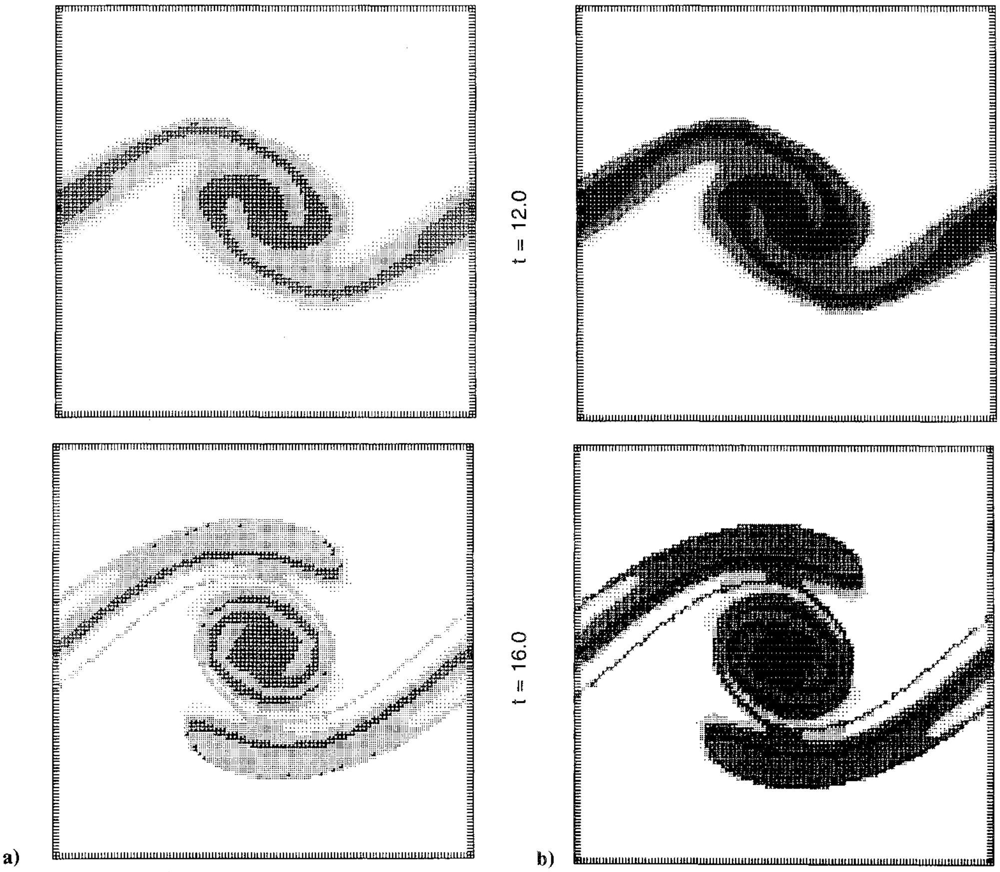

Fig. 7 Contours generated in the x-z plane located at $y = 3.3$ at $t = 12.0$ and 16.0 for a reacting layer with $Da = 0.1$ and $Pe = 1000$: a) product concentration; b) reaction rate.

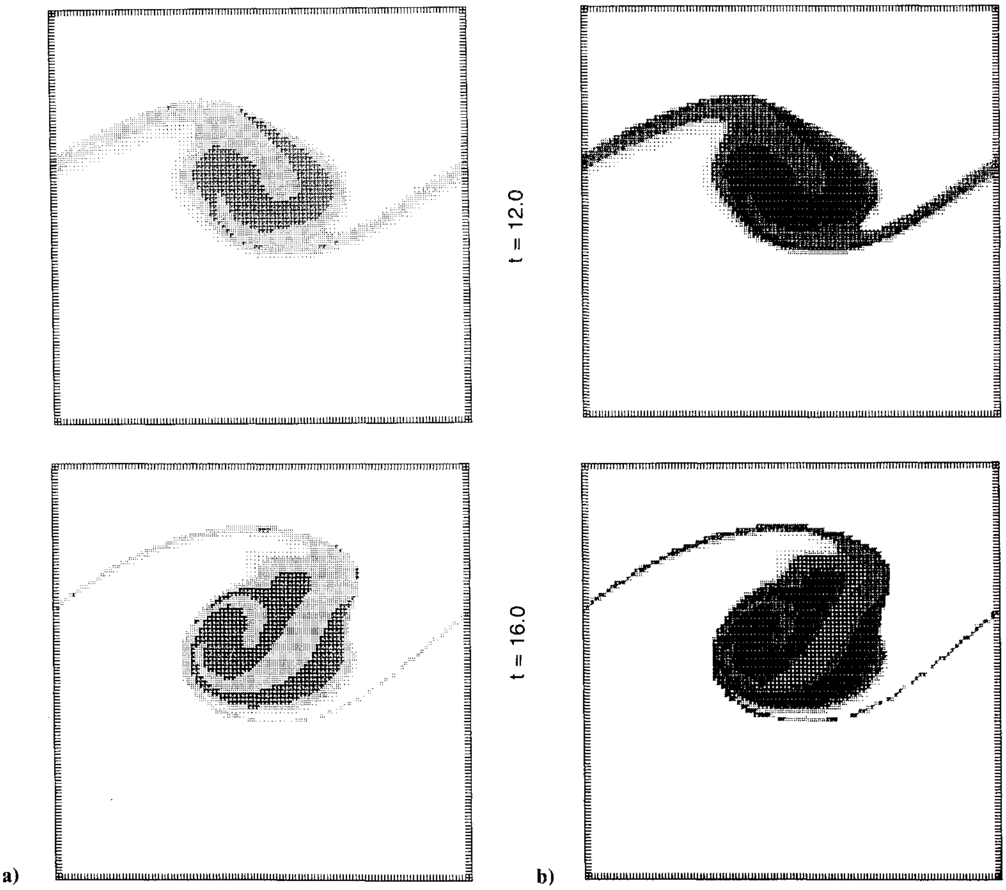

Fig. 8 Contours generated in the x-z plane located at $y = 1.6$ at $t = 12.0$ and 16.0 for a reacting layer with $Da = 0.1$ and $Pe = 1000$: a) product concentration; b) reaction rate.

dimensional simulations in which the strain field of the spanwise vortex cores leads to continuous thinning of the product layer embedded within (or surrounding) the braids.[40]

However, the thinning of the braids and the entrainment of products toward the spanwise vortex core are still observed in the spanwise section $y = 1.6$, which does not intersect any streamwise vortex rod. Meanwhile, the products of reaction undergo a displacement similar to that of the vorticity core (Fig. 8a). The translation of the core toward the top stream and the migration of its geometric center in the opposite direction destroy the symmetry of the product concentration. The asymmetric mixing patterns associated with this mechanism also affect the reaction rate distribution (Fig. 8b) since the reaction rate, which depends strongly on the composition of the reacting mixture, drops rapidly if either oxidizer or fuel become deficient. This description survives the restructuring of the vorticity core by the maturation of three-dimensional instabilities, so that the reaction rate and product concentration distributions at this section are in qualitative agreement with the results of two-dimensional simulations.[40]

The difference between the two sections is directly related to the streamwise vorticity. The presence of streamwise vortex rods leads to mixing and combustion enhancement, a mechanism that resists the negative effects of the underlying two-dimensional strain field. Not only do the streamwise vortex rods lead to mixing enhancement via entrainment, but also maintain high product concentration near their axes (Fig. 7a).

In the streamwise sections, the product concentration changes from a wavy layer across the span into a highly concentrated distribution embedded within the cores of the streamwise vortices. The streamwise vortex rods generate mushroom structures in the braids. With the intensification of the streamwise vorticity in concentrated cores ($t = 16.0$), the field of the vortices causes severe thinning of the "braids" joining neighboring rods which almost become devoid of products. These transverse entrainment currents are best appreciated by simultaneously examining Figs. 10a and 10b, which indicate that the depletion of products occurs despite high reaction rates in regions separating the streamwise eddies. Thus, the strain and entrainment fields tend to reshape the structure of the product concentration such that high product concentration coincides with high concentration of vorticity and falls rapidly as one moves into zones of small vorticity.

The effect of the translation of the spanwise core on the product and reaction rate distributions is inspected in Figs. 9. At early stages, $t \leq 8.0$, combustion occurs in an almost uniform layer across the span. Initial growth of the translative instability causes a wavy deformation of the reaction zone and of the region of high product concentration. The distribution of the latter is complicated by the entrainment of the braids, which trap layers of unburnt fluid on the top and bottom sides of the deformed core. At later stages, the maturation of the three-dimensional instabilities yields distributions of even higher complexity.

The entrainment of mushroom structures formed in the braids toward the cores remains easy to detect. Within these structures, zones of high product coincide with the axes of the corresponding vortex rods while, as expected, reaction rates remain high across the span. The deformation associated with the maturation of the translative instability is harder to analyze, as the core of vorticity crosses the plane of the figure. The streamwise vortices induce a spinning motion that enhances the chemical reaction (Fig. 9b) so that their axes become zones of high product concentration. The motion induced by these vortices, visualized by the redistribution of the reaction zone, resembles the deformation that accom-

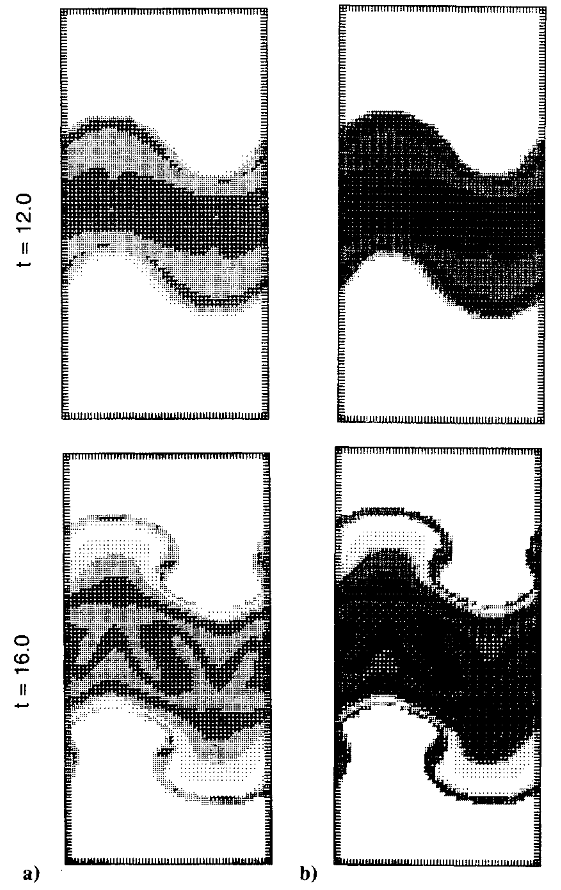

Fig. 9 Contours generated in the y-z plane located at $x = 6.6$ at $t = 12.0$ and 16.0 for a reacting layer with $Da = 0.1$ and $Pe = 1000$: a) product concentration; b) reaction rate.

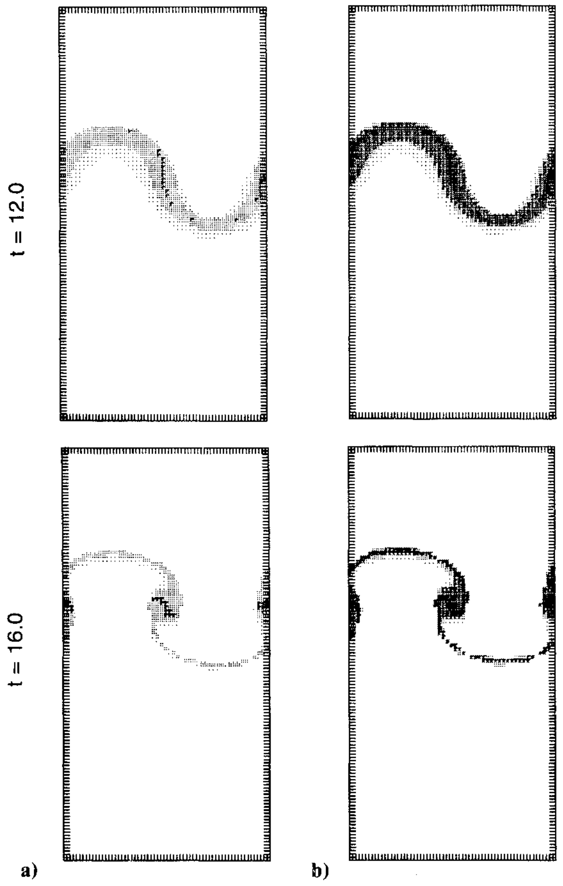

Fig. 10 Contours generated in the y-z plane located at $x = 2.0$ at $t = 12.0$ and 16.0 for a reacting layer with $Da = 0.1$ and $Pe = 1000$: a) product concentration; b) reaction rate.

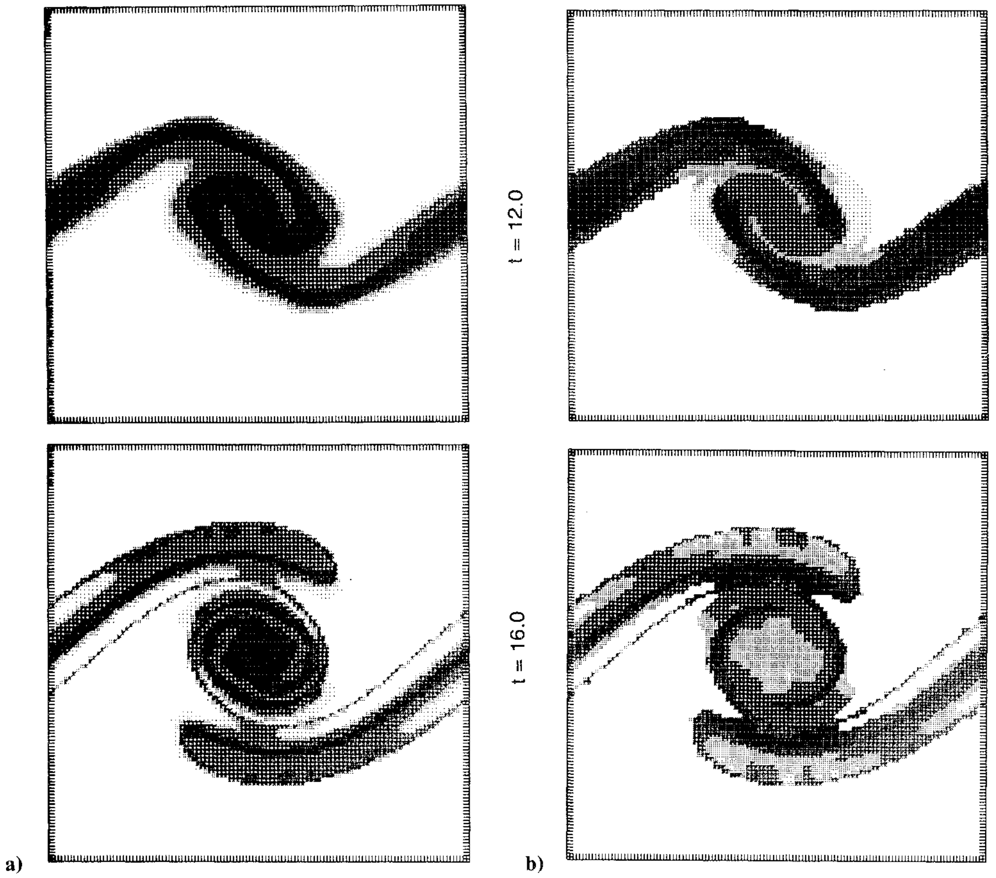

Fig. 11 Contours generated in the x-z plane located at $y = 3.3$ at $t = 12.0$ and 16.0 for a reacting layer with $Da = 10$ and $Pe = 1000$: a) product concentration; b) reaction rate.

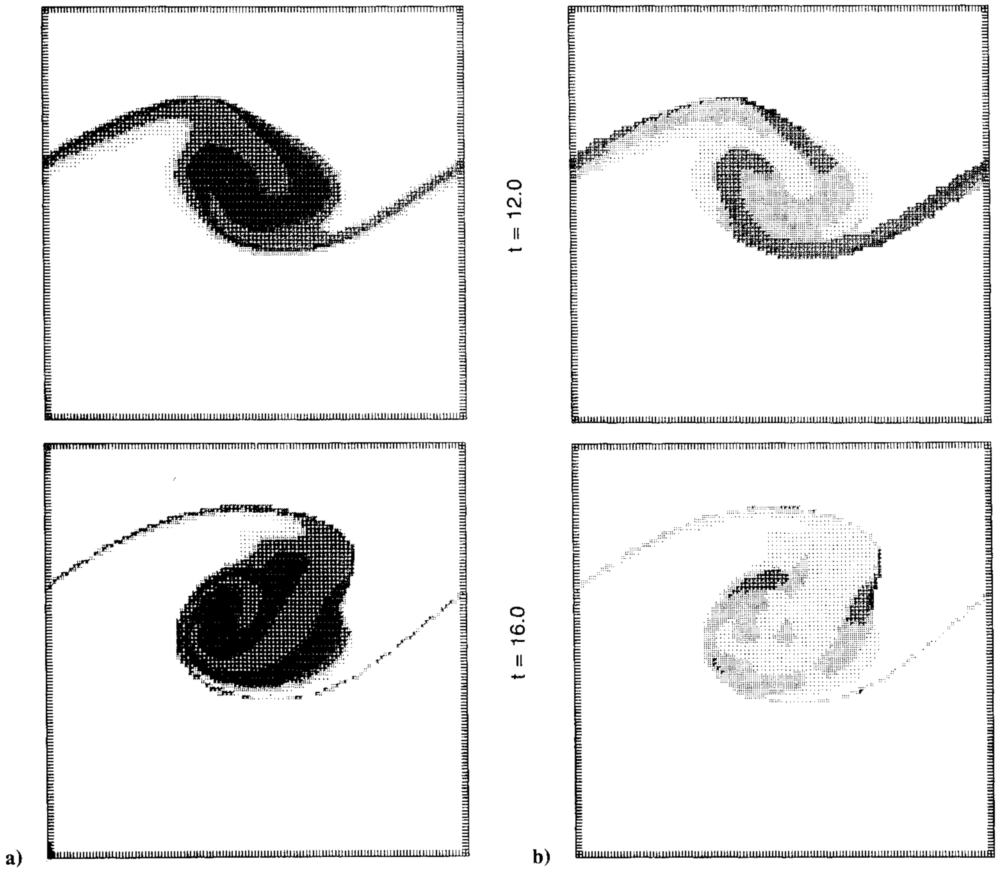

Fig. 12 Contours generated in the x-z plane located at $y = 1.6$ at $t = 12.0$ and 16.0 for a reacting layer with $Da = 10$ and $Pe = 1000$: a) product concentration; b) reaction rate.

panies the formation of the vortex rods and can be predicted by the streamwise vorticity distribution shown in Fig. 5. Interpretation of the product and reaction distributions shown in Fig. 9 requires examination of several sections simultaneously. Such an exercise might be conducted by comparing the distributions of Figs. 8 and 9 with the motion of material particles shown in Figs. 2c and 2b. The comparison yields a clear illustration of the motion of the core of vorticity and of the transverse diffusion fluxes associated with the growth of three-dimensional instabilities.

B. Reacting Layer at High Damkohler Number

We now consider the evolution of the reaction field for a three-dimensional layer at high Damkohler and Peclet numbers, $Da = 10$ and $Pe = 1000$. As in the previous section, the analysis is conducted by plotting the product concentration and normalized reaction rate contours in spanwise and streamwise sections, as can be seen in Figs. 11–14, respectively. In each figure, snapshots of the corresponding variables are shown at $t = 12.0$ and 16.0.

Comparison of Figs. 11a, 12a, 13a, and 14a with their respective counterparts, Figs. 7a, 8a, 9a, and 10a, reveals that the increase in the Damkohler number does not change the structure of the product distribution. Despite high reaction rates, products are reorganized by the flow in such a way as to force a correspondence between zones of high vorticity and high product concentration. This similarity is in agreement with the results of two-dimensional computations.[39,40]

At low Damkohler number, a small reaction rate confines the reaction zone to the initial well-mixed region. At high Damkohler number, the reaction zone undergoes a change as the flow evolves, from a region inside the large cores/rods to a thin zone around their outer boundaries. This is expected since fast reaction rates lead to complete combustion in well-mixed zones and, therefore, to the migration of the reaction zone to reactants-rich regions.

As shown in Fig. 11b, the product concentration reaches values close to one inside the core of the spanwise eddy. Similarly, the section located at $y = 1.6$, shown in Fig. 12b, indicates that the reaction rate drops first at the center of the eddy. At late stages, the reaction zone migrates toward the outer edges of the eddy core. Burning takes place in thin regions located around the outer edges of the core of vorticity, whereas little or no reaction occurs within the core. A similar redistribution of the reaction zone is observed in the spanwise plane $y = 3.3$. However, this effect is less pronounced near the spanwise core, and the braids continue to support the chemical reaction. The difference between the two sections is related to the presence of streamwise vortices whose stirring action results in enhanced transverse diffusion fluxes.

The mechanisms by which the streamwise vortices enhance the rate of burning differ between the core and braid regions. Within the core, streamwise vortices, generated by the deformation of the core itself, cause a spinning motion that is weakly affected by the underlying two-dimensional flow. This results in a limited enhancement in burning rates within a large, product-dominated zone. On the other hand, despite the presence of streamwise vortex rods within the braids, the strain field associated with the underlying two-dimensional flow prevents the formation of a thick product region. Hence, high product concentrations and high reaction rates coexist in this region.

The streamwise sections of Figs. 13b and 14b provide another view of the evolution of the reaction zone in the spanwise direction. At $t = 12.0$, the deformation of the product interfaces is dictated by the growth of three-dimensional instabilities. Combustion occurs in two thin layers enclosing the spanwise vorticity core and in the braids that start to roll under

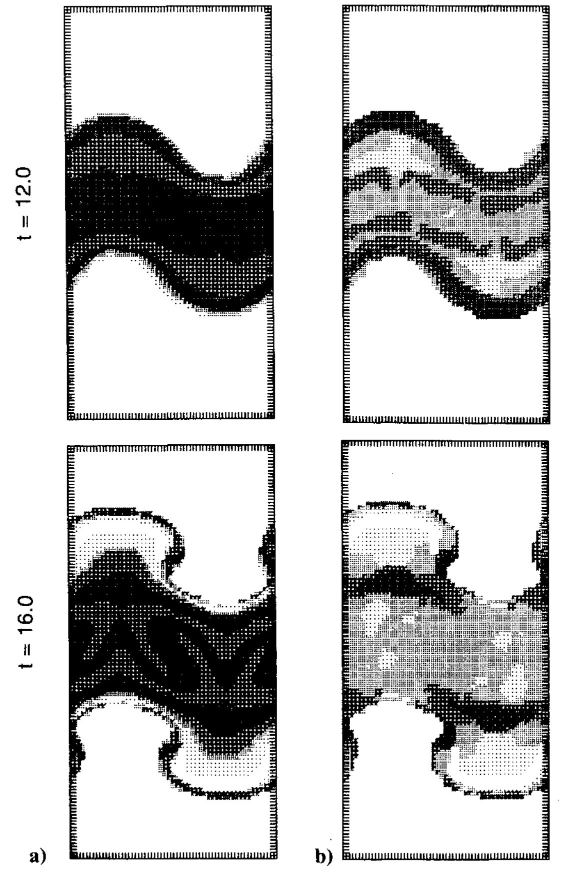

Fig. 13 Contours generated in the y-z plane located at $x = 6.6$ at $t = 12.0$ and 16.0 for a reacting layer with $Da = 10$ and $Pe = 1000$: a) product concentration; b) reaction rate.

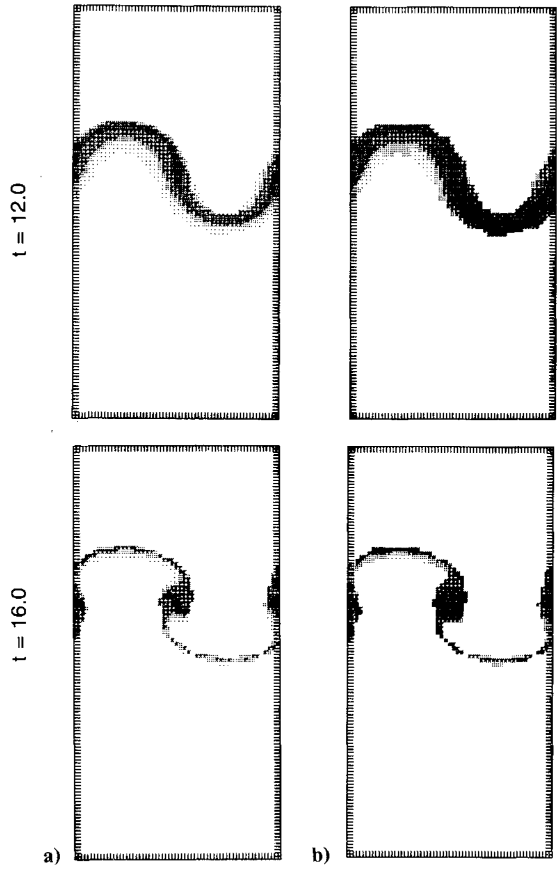

Fig. 14 Contours generated in the y-z plane located at $x = 2.0$ at $t = 12.0$ and 16.0 for a reacting layer with $Da = 10$ and $Pe = 1000$: a) product concentration; b) reaction rate.

the action of the streamwise vortex rods. At later stages, the reaction becomes confined to the core of the vortex rods and a thin layer trapped between the braids and the core region. The region of lowest reaction rate, located within the spanwise core, corresponds to a zone of small streamwise vorticity separating neighboring vortices. On the other hand, cross sections of the braids shown in Fig. 14b confirm our earlier claim regarding the competing influence of the streamwise vortex rods and of the two-dimensional strain field. Despite the extreme thinning of the braids by the strain field of the spanwise core, and the continuous entraiment of the products of reaction, the braids support high reaction rates and high product concentration near the axes of the vortex rods.

C. Total Mass of Products

The evolution of the total mass of products formed,

$$M(t) = \int \rho c_P \, \mathrm{d}\boldsymbol{x} = \sum \rho c_{P,i} \, \mathrm{d}V_i$$

is shown in Figs. 15 for all 21 cases considered. Figures 15 contain three plots corresponding to $Pe = 1000$ (Fig. 15a), $Pe = 500$ (Fig. 15b), and $Pe = 250$ (Fig. 15c), each showing changes in $M(t)$ for seven values of the Damkohler number, $Da = 0.1, 0.2, 0.4, 1.0, 2.5, 5.0$, and 10. Variations in the Peclet number are found to induce minor changes in the product and reaction zone structures. Thus, at high Peclet numbers, the latter are mainly governed by the convective flowfield. However, the reaction rates are strongly dependent on the amount of mixing and, hence, on the coefficients of mass diffusion.

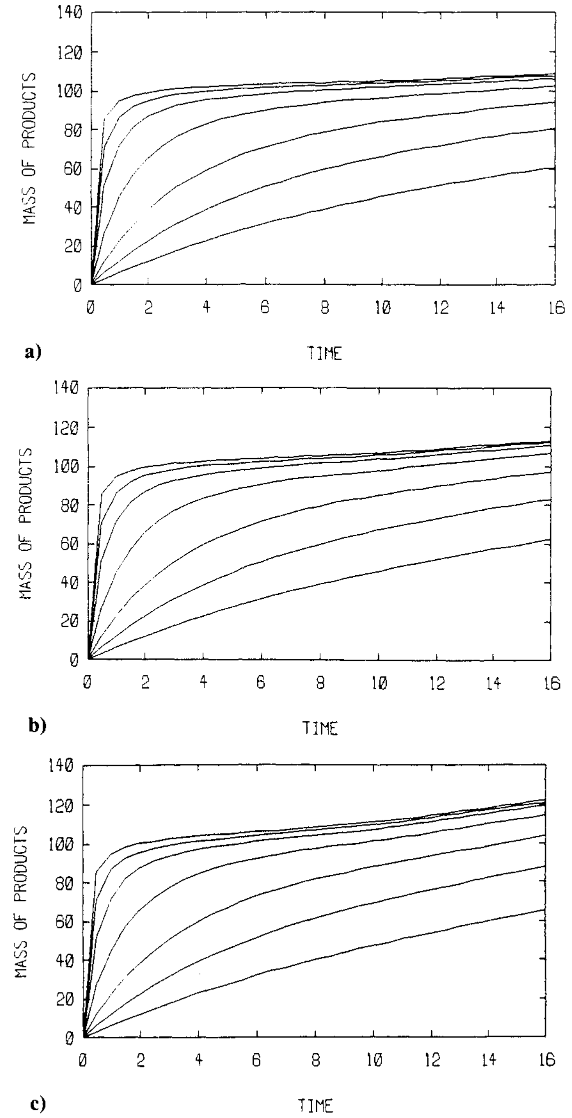

Fig. 15 Evolution of the total mass of products $M(t)$ for reacting shear layers: a) $Pe = 1000$; b) $Pe = 500$; c) $Pe = 250$.

At a high Damkohler number, the chemical reaction leads to an almost immediate and complete burning of the initial mixed region. Curves corresponding to $Da \geq 2.5$ are characterized by a short and sharp initial growth period, which does not depend on the Peclet number. This is expected because, for fast chemistry, regions of mixed reactants burn immediately. An abrupt transition to a controlled growth regime follows, indicating that a diffusion-limited reaction is reached.[41] The buring rates in this regime increase with decreasing Peclet numbers, as indicated by the slopes of the corresponding $M(t)$ curves at later stages between Figs. 15a–c.

At low values of the Damkohler number, $Da \leq 0.4$, the chemical reaction is too slow for such a transition to occur. The evolution of $M(t)$ exhibits a monotonic increase throughout the duration of the computations. As previously mentioned, the reaction remains confined to the initial mixed region. This observation is supported by noting that the mass of products formed at the end of the computations at low Damkohler number is less than that reached at the time of the transition to diffusion-limited regime in the high Damkohler number computations. This explains the fact that, at late stages, the burning rates at low Damkohler number are higher than those at high Damkohler number and that gains in the amount of products formed achieved by decreasing the Peclet number are smaller when the Damkohler number is small.

VI. Conclusions

In this work, the evolution of reacting shear layers are numerically determined in the high Peclet number regime for a wide range of Damkohler numbers. Computed results show that the product distribution is shaped by the convective field induced by spanwise and streamwise vortex structures that form due to the growth of essential instability of the flow. The rollup of spanwise vorticity leads to the creation of concentrated vortex cores and braids that join neighboring cores. Entrainment currents associated with these structures force the migration of products from the braids toward the cores while their induced strain field causes a severe thinning of the braids and of the reaction zone supported therein. However, streamwise vortices, which are generated as a result of growth of three-dimensional instability and are intensified by stretch, significantly affect the flow at later stages, resulting in substantial deviation from the two-dimensional situation.

The maturation of the streamwise vortices into strong streamwise rods and the amplification of the translative instability are accompanied by spanwise variations in the reacting field and the formation of mushroom structures. Mixing and burning enhancement is achieved through the transverse entrainment fluxes. The entrainment fluxes cause a reorganization of the product distribution such that zones of high product concentration always correspond to zones of high magnitude of vorticity. Thus, products tend to migrate toward the core of the spanwise vortices and toward the axes of the streamwise vortex rods.

Although the product distribution is dictated by the flow and is insensitive to variation of the Damkohler number, the structure of the reaction zone depends strongly on the latter. At low Damkohler number, combustion occurs in distributed zones located within the cores of the vortices and is confined to the initial, well-mixed region. As the Damkohler number increases, complete combustion is achieved within the cores of the vortices, thus causing a migration of the reaction zone toward their outer edges. The motion of the reaction zone toward regions of higher strain rates results in a substantial change in its structure as considerable thinning of the latter is observed. Extension of the computations to study pairing among several eddies and to accommodate high heat release, compressible flow models with complex chemical reactions, is currently contemplated.

Acknowledgments

This work was supported by the Air Force Office of Scientific Research Grant AFOSR 84-0356, the National Science Foundation Grant CBT-8709465, and the Department of Energy Grant DE-FG04-87AL44875. Computer support was provided by the John von Neumann National Supercomputer Center.

References

[1]Ghoniem, A. F., Aly, H., and Knio, O. M., "Three-Dimensional Vortex Simulation with Application to Axisymmetric Shear Layer," AIAA Paper 87-0379, Jan. 1987.

[2]Knio, O. M., and Ghoniem, A. F., "On the Formation of Streamwise Vorticity in Turbulent Shear Flows," AIAA Paper 88-0728, Jan. 1988.

[3]Knio, O. M., and Ghoniem, A. F., "Numerical Study of a Three-Dimensional Vortex Method," *Journal of Computational Physics*, Vol. 86, Jan. 1990, pp. 75–106.

[4]Knio, O. M., and Ghoniem, A. F., "Three-Dimensional Vortex Simulation of Entrainment Augmentation Due to Streamwise Vortex Structures," AIAA Paper 89-0574, Jan. 1989.

[5]Knio, O. M., and Ghoniem, A. F., "Three-Dimensional Vortex Simulation of Rollup and Entrainment in a Shear Layer," *Journal of Computational Physics* (to be published).

[6]Bernal, L. P., and Roshko, A., "Streamwise Vortex Structure in Plane Mixing Layers," *Journal of Fluid Mechanics*, Vol. 170, Sept. 1986, pp. 499–525.

[7]Breidenthal, R. E., "A Chemically-Reacting, Turbulent Shear Layer," Ph.D. Dissertation, California Inst. of Technology, Pasadena, CA, 1978.

[8]Jimenez, J., "A Spanwise Structure in the Plane Shear Layer," *Journal of Fluid Mechanics*, Vol. 132, July 1983, pp. 319–336.

[9]Jimenez, J., Cogollos, M., and Bernal, L. P., "A Perspective View of the Plane Mixing Layer," *Journal of Fluid Mechanics*, Vol. 152, March 1985, pp. 125–143.

[10]Lasheras, J. C., and Choi, H., "Three-Dimensional Instability of a Plane Free Shear Layer: An Experimental Study of the Formation and Evolution of Streamwise Vortices," *Journal of Fluid Mechanics*, Vol. 189, April 1988, pp. 53–86.

[11]Michalke, A., "On Spatially Growing Disturbances in an Inviscid Shear Layer," *Journal of Fluid Mechanics*, Vol. 23, Nov. 1965, pp. 521–544.

[12]Pierrehumbert, R. T., and Widnall, S. E., "The Two- and Three-Dimensional Instabilities of a Spatially Periodic Shear Layer," *Journal of Fluid Mechanics*, Vol. 114, Jan. 1982, pp. 59–82.

[13]Riley, J. J., Metcalfe, R. W., and Orszag, S. A., "Direct Numerical Simulation of Chemically-Reacting Turbulent Mixing Layers," *Physics of Fluids*, Vol. 29, Feb. 1986, pp. 406–422.

[14]Riley, J. J., and McMurtry, P. A., "The Use of Direct Numerical Simulation in the Study of Turbulent, Chemically-Reacting Flows," *Turbulent Reactive Flows*, edited by R. Borghi and S. N. B. Murthy, Springer-Verlag, New York, 1989, pp. 486–514.

[15]Lowery, P. S., Reynolds, W. C., and Mansour, N. N., "Passive Scalar Entrainment and Mixing in a Forced Spatially Developing Mixing Layer," AIAA Paper 87-0132, Jan. 1987.

[16]McMurtry, P. A., Riley, J. J., and Metcalfe, R. W., "Effects of Heat Release on the Large-Scale Structure in Turbulent Mixing Layers," *Journal of Fluid Mechanics*, Vol. 199, Feb. 1989, pp. 297–332.

[17]Heidarinejad, G., and Ghoniem, A. F., "Vortex Simulation of the Reacting Shear Layer; Effects of Reynolds and Damkohler Number," AIAA Paper 89-0573, Jan. 1989.

[18]Leonard, A., "Computing Three-Dimensional Incompressible Flows With Vortex Elements," *Annual Review of Fluid Mechanics*, Vol. 17, 1985, pp. 523–559.

[19]Beale, J. T., and Majda, A., "High Order Accurate Vortex Methods with Explicit Velocity Kernels," *Journal of Computational Physics*, Vol. 58, April 1985, pp. 188–208.

[20]Agishtein, M. E., and Migdal, A. A., "Dynamics of Vortex Surface in Three Dimensions: Theory and Simulations," preprint, 1989.

[21]Bathe, K.-J., *Finite Element Procedures in Engineering Analysis*, Prentice-Hall, Englewood Cliffs, NJ, 1982.

[22]Beale, J. T., and Majda, A., "Vortex Methods. I: Convergence in Three Dimensions," *Mathematics of Computation*, Vol. 39, July 1982, pp. 1–27.

[23]Beale, J. T., and Majda, A., "Vortex Methods. II: Higher Order Accuracy in Two and Three Dimensions," *Mathematics of Computation*, Vol. 39, July 1982, pp. 29–52.

[24]Beale, J. T., "A Convergent 3-D Vortex Method With Grid-Free Stretching," *Mathematics of Computation*, Vol. 46, April 1986, pp. 401–424.

[25]Hald, O., "Convergence of Vortex Methods for Euler's Equations. II" *SIAM Journal on Numerical Analysis*, Vol. 16, Oct. 1979, pp. 726–755.

[26]Anderson, C., and Greengard, C., "On Vortex Methods," *SIAM Journal on Numerical Analysis*, Vol. 22, June 1985, pp. 413–440.

[27]Raviart, P. A., "Particle Numerical Models in Fluid Dynamics," *Numerical Methods for Fluid Dynamics II*, edited by K. W. Morton and M. J. Baines, Clarendon, Oxford, England, UK, 1986, pp. 231–253.

[28]Mas-Gallic, S., "Methode Particulaire Pour Une Equation de Convection-Diffusion," *Comptes Rendus de L'Academie des Sciences. Serie I, Mathematique*, Vol. 305, Sept. 1987, pp. 431–434.

[29]Winckelmans, G., and Leonard, A., "Improved Vortex Methods for Three-Dimensional Flows," *Mathematical Aspect of Vortex Dynamics*, edited by R. E. Caflish, Society of Industrial and Applied Mechanics, Philadelphia, PA, 1989, pp. 25–35.

[30]Degond, P., and Mas-Gallic, S., "The Weighted Particle Method for Convection-Diffusion Equations. Part 1: The Case of an Isotropic Viscosity," *Mathematics of Computation*, Vol. 53, Oct. 1989, pp. 485–507.

[31]Degond, P., and Mas-Gallic, S., "The Weighted Particle Method for Convection-Diffusion Equations. Part 2: The Anisotropic Case," *Mathematics of Computation*, Vol. 53, Oct. 1989, pp. 509–525.

[32]Ghoniem, A. F., and Sherman, F. S., "Grid-Free Simulation of Diffusion Using Random Walk Methods," *Journal of Computational Physics*, Vol. 61, Oct. 1985, pp. 1–37.

[33]Ghoniem, A. F., Heidarinejad, G., and Krishnan, A., "Numerical Simulation of a Thermally Stratified Shear Layer Using the Vortex Element Method," *Journal of Computational Physics*, Vol. 79, Nov. 1988, pp. 135–166.

[34]Ashurst, W. T., and Meiburg, E., "Three-Dimensional Shear Layers Via Vortex Dynamics," *Journal of Fluid Mechanics*, Vol. 189, April 1988, pp. 87–116.

[35]Metcalfe, R. W., Orszag, S. A., Brachet, M. E., Menon, S., and Riley, J. J., "Secondary Instability of a Temporally Growing Mixing Layer," *Journal of Fluid Mechanics*, Vol. 184, Nov. 1987, pp. 207–243.

[36]Corcos, G. M., and Lin, S. J., "The Mixing Layer: Deterministic Models of a Turbulent Flow. Part 2. The Origin of the Three-Dimensional Motion," *Journal of Fluid Mechanics*, Vol. 139, Feb. 1984, pp. 67–95.

[37]Lin, S. J., and Corcos, G. M., "The Mixing Layer: Deterministic Models of a Turbulent Flow. Part 3. The Effect of Plane Strain on the Dynamics of Streamwise Vortices," *Journal of Fluid Mechanics*, Vol. 141, April 1984, pp. 139–178.

[38]Widnall, S. E., and Tsai, C.-Y., "The Instability of the Thin Vortex Ring of Constant Vorticity," *Proceedings of the Royal Society of London*, Vol. 287 A1334, Oct. 1977, pp. 273–305.

[39]Ghoniem, A. F., Knio, O. M., and Heidarinejad, G., "The Structure of the Reaction Zone in a Reacting Mixing Layer," *Proceedings of the 12th International Colloquium on Dynamics of Explosions and Reactive Systems*, edited by A. Kuhl (to be published).

[40]Ghoniem, A. F., Knio, O. M., and Krishnan, A., "Lagrangian Simulation of the Initial Stages of a Reacting Jet," *23rd Symposium (International) on Combustion*, The Combustion Institute, Pittsburgh, PA, 1990, pp. 699–705.

[41]Mungal, M. G., and Frieler, C. E., "The Effects of Damkohler Number in a Turbulent Shear Layer," *Combustion and Flame*, Vol. 71, Jan. 1988, pp. 23–34.